Impact of spin in compact binary foreground subtraction for estimating the residual stochastic gravitational-wave background in ground-based detectors

Hanlin Song,[1] Dicong Liang,[2,3] Ziming Wang,[2] and Lijing Shao[2,4,*]

[1]*School of Physics, Peking University, Beijing 100871, China*
[2]*Kavli Institute for Astronomy and Astrophysics, Peking University, Beijing 100871, China*
[3]*Department of Mathematics and Physics, School of Biomedical Engineering, Southern Medical University, Guangzhou 510515, China*
[4]*National Astronomical Observatories, Chinese Academy of Sciences, Beijing 100012, China*

(Received 1 January 2024; accepted 13 May 2024; published 7 June 2024)

Stochastic gravitational-wave (GW) background (SGWB) contains information about the early Universe and astrophysical processes. The recent evidence of SGWB by pulsar timing arrays in the nanohertz band is a breakthrough in the GW astronomy. For ground-based GW detectors, while in data analysis, the SGWB can be masked by loud GW events from compact binary coalescences (CBCs). Assuming a next-generation ground-based GW detector network, we investigate the potential for detecting the astrophysical and cosmological SGWB with non-CBC origins by subtracting recovered foreground signals of loud CBC events. The Fisher Information Matrix (FIM) method is adopted for quick calculation. As an extension of the previous studies, two more essential features are considered. Firstly, we incorporate nonzero aligned or antialigned spin parameters in our waveform model. Because of the inclusion of spins, we obtain significantly more pessimistic results than the previous work, where the residual energy density of foreground is even larger than the original CBC foreground. For the most extreme case, we observe that the subtraction results are approximately 10 times worse for binary black hole events and 20 times worse for binary neutron star events than the scenarios without accounting for spins. The degeneracy between the spin parameters and the symmetric mass ratio is strong in the parameter estimation process, and it contributes most to the imperfect foreground subtraction. Secondly, in this work, extreme CBC events with condition numbers of FIMs $c_\Gamma > 10^{15}$ are preserved. The impacts of these extreme events on foreground subtraction are discussed. Our results have important implications for assessing the detectability of SGWB from non-CBC origins for ground-based GW detectors.

DOI: 10.1103/PhysRevD.109.123014

I. INTRODUCTION

Recently, intriguing evidence of the Hellings-Downs correlation [1] for gravitational-wave (GW) signals in the nanohertz band were revealed by several pulsar timing arrays (PTAs), including the North American Nanohertz Observatory for Gravitational waves [2,3], the European PTA, along with the Indian PTA [4–6], the Parkes PTA [7,8], and the Chinese PTA [9]. These signals might have originated from the stochastic GW background (SGWB). Broadly speaking, the SGWB may arise from multiple origins, including cosmological and astrophysical phenomena [10]. Possible cosmological origins include inflation [11], cosmic strings [12,13], first-order phase transitions [14–18], and so on. Astrophysical origins include asymmetry of supernovae [19], core collapse of supernovae [20], cumulative effects of compact binary coalescences (CBCs) [21–25], and so on.

At present, the ground-based GW detector network is searching for signals from both astrophysical and cosmological SGWB in the audio frequency band. The cross-correlation method is adopted, which assumes the SGWB is correlated between detectors while instrument noise is not correlated [26,27]. After processing the data from the three observing runs (O1, O2, and O3) of LIGO/Virgo/KAGRA detectors, no evidence for SGWB was found [28]. To detect a persistent signal from the SGWB, one needs long-term observation to improve the sensitivity. However, during such an observation, a considerable number of CBC events form a loud foreground, weakening the ability to detect the SGWB from other origins. Currently, nearly one hundred CBC events are published in the first three observing runs of the LIGO/Virgo/KAGRA (LVK) Collaboration [29–34]. In the future, with the deployment of the next-generation (XG) ground-based detectors, including the Einstein

*lshao@pku.edu.cn

 © 2024 American Physical Society

Telescope (ET) [35,36] and the Cosmic Explorer (CE) [37,38], thousands of CBC events will be detected annually [39–41]. In this work, we are interested in exploring the prospect of observing the non-CBC origin SGWB with the XG ground-based GW detector network. Therefore, one needs to carefully deal with this foreground composed of CBC events [21,22,42–47].

Previously, Sachdev *et al.* [43] considered the detection of SGWB of non-CBC origin in a network of XG detectors. They adopted the Fisher Information Matrix (FIM) method to quickly estimate the residual background after subtracting the resolved CBC events. For both binary black hole (BBH) and binary neutron star (BNS) events, Sachdev *et al.* [43] used a post-Newtonian (PN) expansion waveform with only three free binary parameters, i.e., the coalescence time t_c, the coalescence phace ϕ_c, and the chirp mass $\mathcal{M}$. They found that the residual background from BNS events is too large, limiting the capability of observing SGWB from non-CBC origins, while the signals from BBH events can be subtracted sufficiently such that their effect is negligible. However, a recent study by Zhou *et al.* [44] showed pessimistic results. They adopted the same method as Sachdev *et al.* [43] but added another six free parameters that are normal in real parameter estimation (PE[1]) of CBCs, including the symmetric mass ratio η, the redshift z, the right ascension α, the declination δ, the orbital inclination angle ι, and the GW polarization angle ψ. For simplicity, Zhou *et al.* [44] have set the spins to zero for all CBC events and adopted the `IMRPhenomC` and `IMRPhenomD` models to generate waveforms. They found that including more parameters leads to a significantly larger residual background for both BBH and BNS events than what was found by Sachdev *et al.* [43]. This is mainly due to the degeneracy between the luminosity distance D_L and the orbital inclination angle ι, as well as the degeneracy between the coalescence phase ϕ_c and the polarization angle ψ. There are also other methods for further foreground subtraction, such as Cutler and Harms [21] and Pan and Yang [46]. For the method of measuring the SGWB without subtracting the foreground, readers are referred to Biscoveanu *et al.* [48].

In this work, we consider two more essential features built upon the subtraction methods in Sachdev *et al.* [43] and Zhou *et al.* [44]. Firstly, the nonzero spins aligned or antialigned with the orbital angular momentum in the waveform are considered. Common envelope evolution theory predicts that BBH events have nearly aligned spins [49–55]. Meanwhile, the majority of observed BBH events in the Gravitational Wave Transient Catalog 3 (GWTC-3) preferentially have aligned spins, and evidence of events with antialigned spins is also observed [56]. For BNS events, the spin axis will become aligned with orbital angular momentum during the evolution of neutron star recycling [57,58]. Moreover, from the perspective of post-Newtonian expansion of the GW waveform, aligned spins are the dominant contribution from spins to the phasing of GWs, and the degeneracy between spins and symmetric mass ratio appears at 1.5 PN order, which could lead to large uncertainty in PE. Therefore, spin effects need to be considered in a more realistic CBC foreground subtraction scenario. Secondly, we adopt the FIM to get a quick estimation. When degeneracy arises from two parameters in the waveform, the FIM will be nearly singular, which corresponds to an extremely high value of c_Γ [59,60]. In the literature, those extreme events were arbitrarily discarded to ensure numerical precision when calculating the inverse of FIM [59,61]. Here, this precision problem is solved with the help of the arbitrary-precision floating-point tool `mpmath` [62]. Therefore, those extreme events are preserved in our simulation. We discuss the effects of these extreme events on foreground subtraction.

In this work, we first generate a population of 10^5 BBH events and 10^5 BNS events up to a redshift of $z \sim 10$.[2] Then, we employ an 11-dimensional PE (11-d) PE for these BBH and BNS events using the FIM method. Comparing the results to those from the nine-dimensional PE (9-d) by Zhou *et al.* [44], we find that the residual of the foreground becomes even larger than the original background, which is primarily due to the degeneracy between the spin parameters and the symmetric mass ratio. These results have significant implications for assessing the detectability of SGWB from non-CBC origins for ground-based GW detectors.

This paper is arranged as follows. In Sec. II, we introduce the basics of the work, including the definition of the energy density spectrum of GW events and the subtraction methods. Also, we present our simulation methods for generating BBH and BNS populations, the configuration of an XG detector network, and the PE methods used in this work. In Sec. III, we illustrate our results and compare them with earlier results. The discussion is presented in Sec. IV.

II. SETTINGS AND METHODS

In this section, we present our settings for the calculation and the consideration behind these settings. We also explicitly spell out the details of our methods in the calculation.

[1]Here in this work, we use PE to mean that, when the signal-to-noise ratio of an event is large enough, the FIM method is adopted to obtain a multivariate Gaussian distribution to mimic the posterior. Afterward we use this posterior to draw samples. It is distinct from the normal PE studies in real GW data.

[2]A more complete treatment can include neutron star–black hole binaries as well [22]. Here, we use BNSs and BBHs to contrast our results with those of Sachdev *et al.* [43] and Zhou *et al.* [44].

A. CBC population model

Neglecting the tidal effects and detailed ringdown signals in BNSs, a generic spinning, nonprecessing, circular GW waveform is described by 11 parameters and can be generated by the `IMRPhenomD` model [63,64]. Zhou *et al.* [44] considered nine free parameters and fixed both spins to zero. In a PE process, it is more realistic to include the spin effects. Ideally, we shall consider generic spins, but here we restrain ourselves to aligned spins only which contribute most significantly in the GW phasing. Therefore, we consider two more free parameters than Zhou *et al.* [44], which are spins aligned or antialigned with the orbital angular momentum. The 11 free parameters we consider are

$$\boldsymbol{\theta} = \{m_1, m_2, D_L, \alpha, \delta, \iota, \psi, \phi_c, t_c, \chi_{1z}, \chi_{2z}\}, \tag{1}$$

where m_1 and m_2 are masses of the two components, and χ_{1z} and χ_{2z} are spins paralleled with the orbital angular momentum.

In our simulation, 10^5 events are generated for BBHs and BNSs, respectively. The population models are chosen as follows. Angle parameters such as α, ψ, and ϕ_c are drawn from a uniform distribution, $\mathcal{U}[0, 2\pi)$, while $\cos\iota$ and $\cos\delta$ are drawn from $\mathcal{U}[-1, 1]$. For the coalescence time, without losing generality, we set $t_c = 0$, but still include it in the parameter estimation.

For the luminosity distance which is generated from redshift, we first consider the local merger rate in the comoving coordinates,

$$R_m(z_m) = \int_{t_d^{\min}}^{t_d^{\max}} R_{\rm sf}\{z[t(z_m) - t_d]\}p(t_d)\mathrm{d}t_d, \tag{2}$$

where $t(z_m)$ represents the cosmic time at merger at redshift z_m, and $R_{\rm sf}$ is the star-formation rate for binary systems whose details can be found in Ref. [65]. Additionally, t_d denotes the time delay between binary formation and merger, assumed to follow the distribution [51,51,66–70],

$$p(t_d) \propto \frac{1}{t_d}, \qquad t_d^{\min} < t_d < t_d^{\max}, \tag{3}$$

where $t_d^{\max}$ is selected to be equal to the Hubble time, and

$$t_d^{\min} = \begin{cases} 20\ \text{Myr}, & \text{for BNSs}, \\ 50\ \text{Myr}, & \text{for BBHs}. \end{cases} \tag{4}$$

Moreover, heavy BBHs are more likely to be formed in a low-metallicity environment [68]. When BBHs have the mass of at least one black hole greater than $30M_\odot$, the star-formation rate in Eq. (2) needs to be modified into [71]

$$R_{\rm BBH}(z) \propto R_{\rm sf}(z) * F(z), \tag{5}$$

where

$$F(z) = \frac{\int_{-\infty}^{\log Z_\odot/2} \exp\{-2[\log Z - \overline{\log Z(z)}]^2\} d\log Z}{\int_{-\infty}^{\infty} \exp\{-2[\log Z - \overline{\log Z(z)}]^2\} d\log Z}, \tag{6}$$

with the metallicity of the Sun $Z_\odot = 0.02$; the detail of $\overline{\log Z(z)}$ can be found in Callister *et al.* [71].

The distribution of redshift is obtained from the merger rate in the observer frame [51,71],

$$R_z(z) = \frac{R_m(z)}{1+z}\frac{\mathrm{d}V_c(z)}{\mathrm{d}z}. \tag{7}$$

For BBH mass parameters, we adopt the "POWER LAW + PEAK" mass model based on GWTC-3 [56,72]. The primary mass follows a truncated power-law distribution, supplemented by a Gaussian component,

$$P(m_1) \propto S(m_1|m_{\min}, \delta_m)[(1-\lambda_{\rm peak})P_{\rm law}(m_1|-\alpha, m_{\max}) + \lambda_{\rm peak}\mathcal{N}(\mu_m, \sigma_m)], \tag{8}$$

where $\alpha = 3.14$ and $m_{\max} = 86.85M_\odot$ for the power-law component, $\mu_m = 33.73M_\odot$ and $\sigma_m = 3.36M_\odot$ for the Gaussian component, and $m_{\min} = 5.08M_\odot$ and $\delta_m = 4.83M_\odot$ for the smoothing function $S(\cdot|\cdot)$ [56]. The weight parameter $\lambda_{\rm peak} = 0.038$ is chosen as by Abbott *et al.* [56]. The secondary mass population is sampled from a conditional mass distribution over mass ratio $q = m_2/m_1$ [56,72],

$$p(q) \propto q^{\gamma_q} S(m_2|m_{\min}, \delta_m), \tag{9}$$

where $\gamma_q = 1.08$.

For BNSs, the mass model is adopted from Farrow *et al.* [73]. The primary mass m_1 is sampled from a double Gaussian distribution,

$$P(m_1) = \gamma_{\rm NS}\mathcal{N}(\mu_1, \sigma_1) + (1-\gamma_{\rm NS})\mathcal{N}(\mu_2, \sigma_2), \tag{10}$$

with $\gamma_{\rm NS} = 0.68$, $\mu_1 = 1.34M_\odot$, $\sigma_1 = 0.02M_\odot$, $\mu_2 = 1.47M_\odot$, and $\sigma_2 = 0.15M_\odot$. The secondary mass m_2 follows a uniform distribution, $\mathcal{U}[1.14M_\odot, 1.46M_\odot]$.

As for the spin parameters, we assume χ_{1z} and χ_{2z} to follow a uniform distribution $\mathcal{U}[-1, 1]$ for BBHs, and follow a Gaussian distribution $\mathcal{N}(\mu_\chi, \sigma_\chi)$ with $\mu_\chi = 0$ and $\sigma_\chi = 0.05$ for BNSs [74].

B. Waveform reconstruction

For large populations, the computational cost is expensive if one conducts a full Bayesian PE for each event [75]. Similarly to Sachdev *et al.* [43] and Zhou *et al.* [44], we adopt the FIM method to recover parameters and their

uncertainties. We reconstruct waveforms from the FIM results for both BBH and BNS events.

Assuming that the noise is stationary and Gaussian, under the linear-signal approximation, the posterior distribution of GW parameters is [61,76]

$$p(\boldsymbol{\theta}) \sim \mathrm{e}^{-\frac{1}{2}\Gamma_{ij}\Delta\theta_i\Delta\theta_j}, \tag{11}$$

where Γ_{ij} is the FIM,

$$\Gamma_{ij} \equiv \langle \partial_{\theta_i} H(\boldsymbol{\theta}; f), \partial_{\theta_j} H(\boldsymbol{\theta}; f) \rangle, \tag{12}$$

where $H(\boldsymbol{\theta}; f)$ is the strain recorded in the detector, and the inner product for two quantities $A(\boldsymbol{\theta}; f)$ and $B(\boldsymbol{\theta}; f)$ is defined as

$$\langle A, B \rangle = 2 \int_0^\infty \mathrm{d}f \frac{A(\boldsymbol{\theta}; f) B^*(\boldsymbol{\theta}; f) + A^*(\boldsymbol{\theta}; f) B(\boldsymbol{\theta}; f)}{S_n(f)}, \tag{13}$$

where $S_n(f)$ is the one-side power spectrum density (PSD) for a specific detector.

For a detected event, its matched-filter signal-to-noise ratio (SNR) is defined as $\rho = \sqrt{\langle H, H \rangle}$. Then for a network with N_d detectors, the corresponding SNR and FIM are respectively,

$$\rho_{\mathrm{net}} = \sqrt{\sum_{i=1}^{N_d} \rho_i^2}, \qquad \Gamma_{\mathrm{net}} = \sum_{i=1}^{N_d} \Gamma_i. \tag{14}$$

We consider three XG detectors, including one CE with a 40-km arm length located in Idaho, U.S., one CE with a 20-km arm length located in New South Wales, Australia, and one ET with a triangular configuration located in Cascina, Italy. This detector network corresponds to the fiducial scenario used by Zhou *et al.* [44].

After obtaining the FIM of 11 free parameters for each CBC event, we utilize $\boldsymbol{\theta}^i_{\mathrm{tr}}$ and the covariance matrix $\Sigma_{\mathrm{net}} \equiv \Gamma^{-1}_{\mathrm{net}}$ to construct a multivariate Gaussian distribution. Subsequently, we employ this distribution to randomly draw in the 11-d parameter space to mimic the recovered GW parameters, $\boldsymbol{\theta}^i_{\mathrm{rec}}$, which are employed to generate the reconstructed GW waveforms, $\tilde{h}_+(\boldsymbol{\theta}^i_{\mathrm{rec}}; f)$ and $\tilde{h}_\times(\boldsymbol{\theta}^i_{\mathrm{rec}}; f)$. We use the `GWBENCH` package (version `0.7.1`) [61] to obtain the PSDs, generate the GW waveforms, and calculate SNRs and FIMs.

It is worth noting that Eq. (11) is a good approximation for high SNR events [60]. In principle, one should conduct a full Bayesian analysis for more accurate results, at least for those low SNR events where FIM is not applicable. In this work, we are more interested in a fast order-of-magnitude estimate for the CBC foreground subtraction. Therefore, we adopt the FIM method for 10^5 events as a compromise solution considering the accuracy and computational expense.

C. Foreground subtraction methods

The dimensionless energy density spectrum of GW, Ω_{GW}, is defined as [24]

$$\Omega_{\mathrm{GW}}(f) := \frac{f}{\rho_c c} F(f), \tag{15}$$

where $F(f)$ is the energy flux, $\rho_c = (3c^2 H_0^2)/(8\pi G)$ is the critical energy density, and H_0 is the Hubble constant. The total flux of N CBC sources is given by [24]

$$F_{\mathrm{tot}} = \frac{\pi c^3}{2G} \frac{f^2}{T} \sum_{i=1}^{N} [|\tilde{h}^i_+(\boldsymbol{\theta}^i_{\mathrm{tr}}; f)|^2 + |\tilde{h}^i_\times(\boldsymbol{\theta}^i_{\mathrm{tr}}; f)|^2], \tag{16}$$

where $\tilde{h}^i_+(\boldsymbol{\theta}^i_{\mathrm{tr}}; f)$ and $\tilde{h}^i_\times(\boldsymbol{\theta}^i_{\mathrm{tr}}; f)$ are plus and cross modes of GWs from the ith CBC event in the frequency domain, and T corresponds to the total duration of the observation.

To detect the SGWB from non-CBC origins with the XG ground-based GW detector network, we need to verify how well the CBC foreground can be subtracted. If the subtraction performs well so that the residual spectrum Ω_{res} is much smaller than the spectrum from a non-CBC origin SGWB, then it might be detected on the XG detector network. During the subtraction, the Ω_{res} comes from two parts:

$$\Omega_{\mathrm{res}} = \Omega_{\mathrm{ns}} + \Omega_{\mathrm{err}}, \tag{17}$$

where Ω_{ns} comes from those weak events which cannot be resolved by the network, and Ω_{err} comes from the imperfect subtraction of detected events.

Following Zhou *et al.* [44], a threshold SNR ρ_{thr} is used to divide all the CBC events into two groups: those to be subtracted and those not to be subtracted. We denote N_{s} (N_{ns}) as the number of CBC events whose ρ_{net} is greater (less) than ρ_{thr}. Thus, the energy flux of the N_{ns} CBC events which are not to be subtracted is

$$F_{\mathrm{ns}} = \frac{\pi c^3}{2G} \frac{f^2}{T} \sum_{i=1}^{N_{\mathrm{ns}}} [|\tilde{h}^i_+(\boldsymbol{\theta}^i_{\mathrm{tr}}; f)|^2 + |\tilde{h}^i_\times(\boldsymbol{\theta}^i_{\mathrm{tr}}; f)|^2]. \tag{18}$$

For the other N_{s} events which need to be subtracted, we first reconstruct the waveform $\tilde{h}^i_\times(\boldsymbol{\theta}^i_{\mathrm{tr}}; f)$. This step is done by the FIM method mentioned in Sec. II B. Owing to the existence of noise, there always is a mismatch between θ^i_{tr} and θ^i_{rec}. Thus, a residual strain for each N_{s} event will be left in the data during the subtraction:

$$\delta\tilde{h}^i_{+/\times} = \tilde{h}^i_{+/\times}(\boldsymbol{\theta}^i_{\mathrm{tr}}; f) - \tilde{h}^i_{+/\times}(\boldsymbol{\theta}^i_{\mathrm{rec}}; f). \tag{19}$$

This will finally contribute to the Ω_{res} as imperfect subtraction part Ω_{err}. The corresponding energy flux of the residual strain is

$$F_{\rm err} = \frac{\pi c^3}{2G}\frac{f^2}{T}\sum_{i=1}^{N_s}[|\delta\tilde{h}^i_+|^2 + |\delta\tilde{h}^i_\times|^2]. \quad (20)$$

In our simulation, the main work involves calculating the $\Omega_{\rm ns}$ and $\Omega_{\rm err}$ of our CBC population based on the FIM method. There are also other ways to calculate $\Omega_{\rm err}$ by Eq. (A4) [21,46] in which one subtracts the reconstructed strain from the true strain recorded in the detector. As shown in the Appendix, the effects of subtraction of these two methods are in the same order, especially when the spin effects are considered.

III. RESULTS

When we try to obtain the covariance matrix through numerical inversion, there is a condition number, c_Γ, defined as the ratio between the largest eigenvalue and smallest one, which limits the accuracy of the numerical inversion of the FIM. As was pointed out by Borhanian [61], when using `GWBENCH 0.65` to calculate the covariance matrix, the inversion is not reliable when c_Γ exceeds 10^{15}. This is because the commonly used `float64` format in the computer only guarantees about 15 significant decimal digits. However, when two parameters are highly degenerate in the waveform, the FIM will be nearly singular, which leads to a high value c_Γ [59]. For some extreme events in our simulated population, the value of c_Γ will exceed 10^{15} while for the latest version `0.7.1`, `GWBENCH` uses the `mpmath` [62] routine to ensure the accuracy of numerical inversion based on the value of c_Γ. Specifically, the floating-point numbers used in `mpmath` are represented as a four-tuple (*sign*, *man*, *exp*, *bc*). The first three components are the sign, the *mantissa*, and the *exponent*, and they are normally used to save a number in

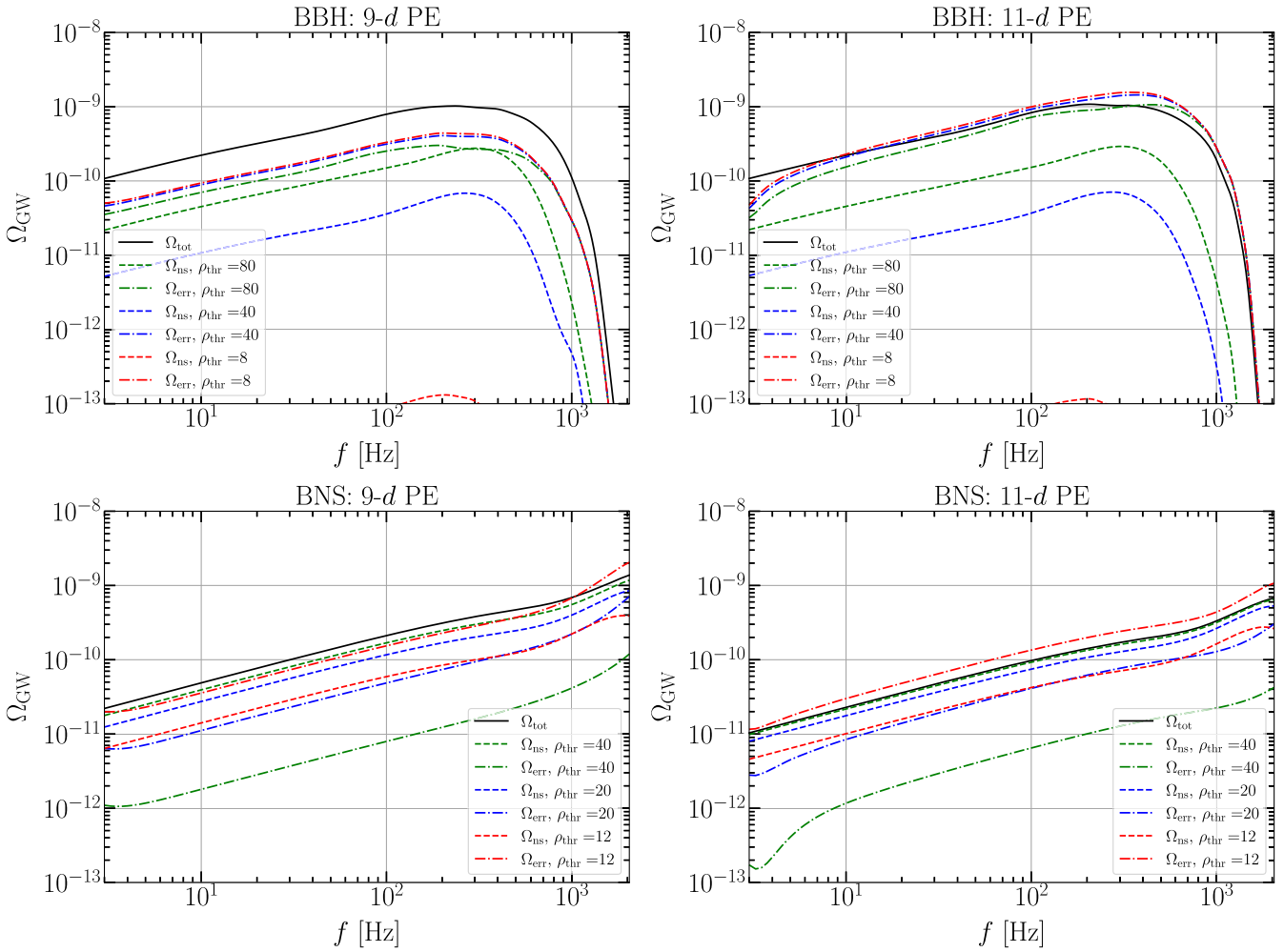

FIG. 1. Results from TREATMENT (I) for 9-*d* PE for BBHs (upper left) and BNSs (lower left), and 11-*d* PE for BBHs (upper right) and BNSs (lower right). Each subfigure shows the total GW energy spectrum $\Omega_{\rm tot}$ in black solid line and two components ($\Omega_{\rm ns}$ and $\Omega_{\rm err}$) of the residual GW energy spectrum for different $\rho_{\rm thr}$. $\Omega_{\rm ns}$ (dashed line) comes from the events that are not subtracted while $\Omega_{\rm err}$ (dash-dotted line) comes from the imperfect subtraction of the CBC foreground. For a direct check, the two panels on the left reproduce the results of Fig. 2 in Zhou *et al.* [44] for the `IMRPhenomD` waveform.

the computer as $(-1)^{\text{sign}} \times \text{man} \times 2^{\text{exp}}$. The last component, the *bitcount*, is the newly defined parameter for saving the size of the absolute value of the mantissa in bits. The precision, *prec*, for the float number depends on the maximum allowed *bc* as 2^{prec} [62]. Compared to the default prec = 11 in *float*64 number, the components in FIM saved in `mpmath` can be set to high numerical precision according to the value of c_Γ. Therefore, we keep all those events with a large condition number in our simulations, rather than disregarding them completely as mentioned in [59].

Owing to the different treatments of events with large condition number c_Γ, and for a consistency check with previous work [44], we employ two analysis treatments in the following discussion: for TREATMENT (I) we subtract the events whose $\rho_{\text{net}} > \rho_{\text{thr}}$ and $c_\Gamma < 10^{15}$ and for TREATMENT (II) we subtract the events as long as their $\rho_{\text{net}} > \rho_{\text{thr}}$. TREATMENT (I) is consistent with the treatment in the previous version of `GWBENCH` which was adopted by Zhou *et al.* [44], while TREATMENT (II) is consistent with the specifics in the version `0.7.1` of `GWBENCH`.

We here consider four PE cases in our calculation:

(i) 9-*d* PE for 10^5 BBH events,
(ii) 9-*d* PE for 10^5 BNS events,
(iii) 11-*d* PE for 10^5 BBH events,
(iv) 11-*d* PE for 10^5 BNS events.

The parameter configuration of the first two cases is the same as in Zhou *et al.* [44] for validation and comparison reasons. The results of these four cases from TREATMENT (I) are shown in Fig. 1, and from TREATMENT (II) are shown in Fig. 2. In each figure, the left panels show the results of 9-*d* PE for BBH and BNS events, while the right panels show the results for 11-*d* PE cases. We denote the spectrum Ω_{tot} with a solid black line. Then, we choose three different ρ_{thr}, i.e., $\rho_{\text{thr}} = 8, 40, 80$ for BBH events, and $\rho_{\text{thr}} = 12, 20, 40$ for BNS events. For each ρ_{thr}, we denote the spectrum Ω_{ns} with a dashed line and the spectrum Ω_{err} with a dash-dotted line. The left panels of both figures reproduce well the

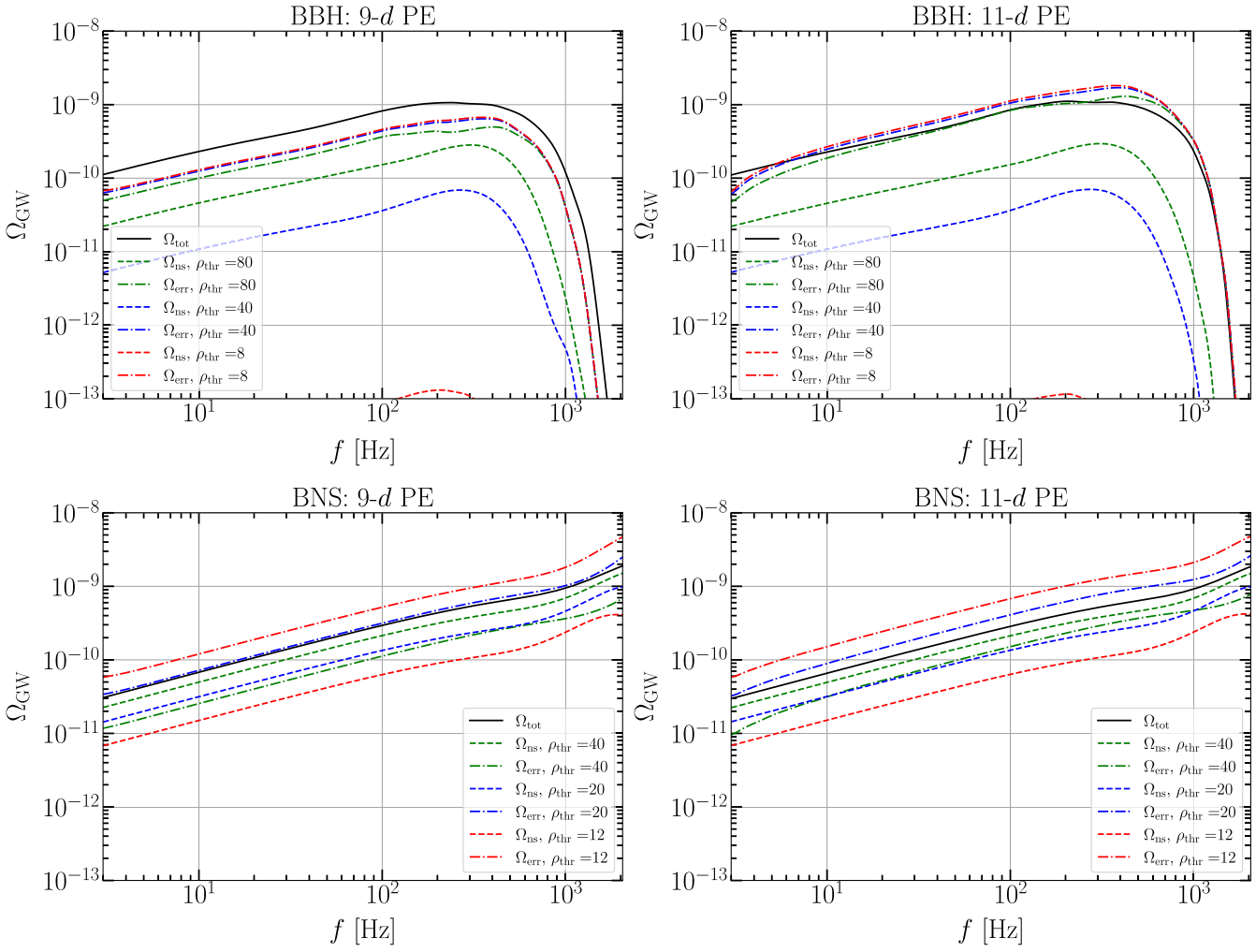

FIG. 2. Same as Fig. 1, but for TREATMENT (II).

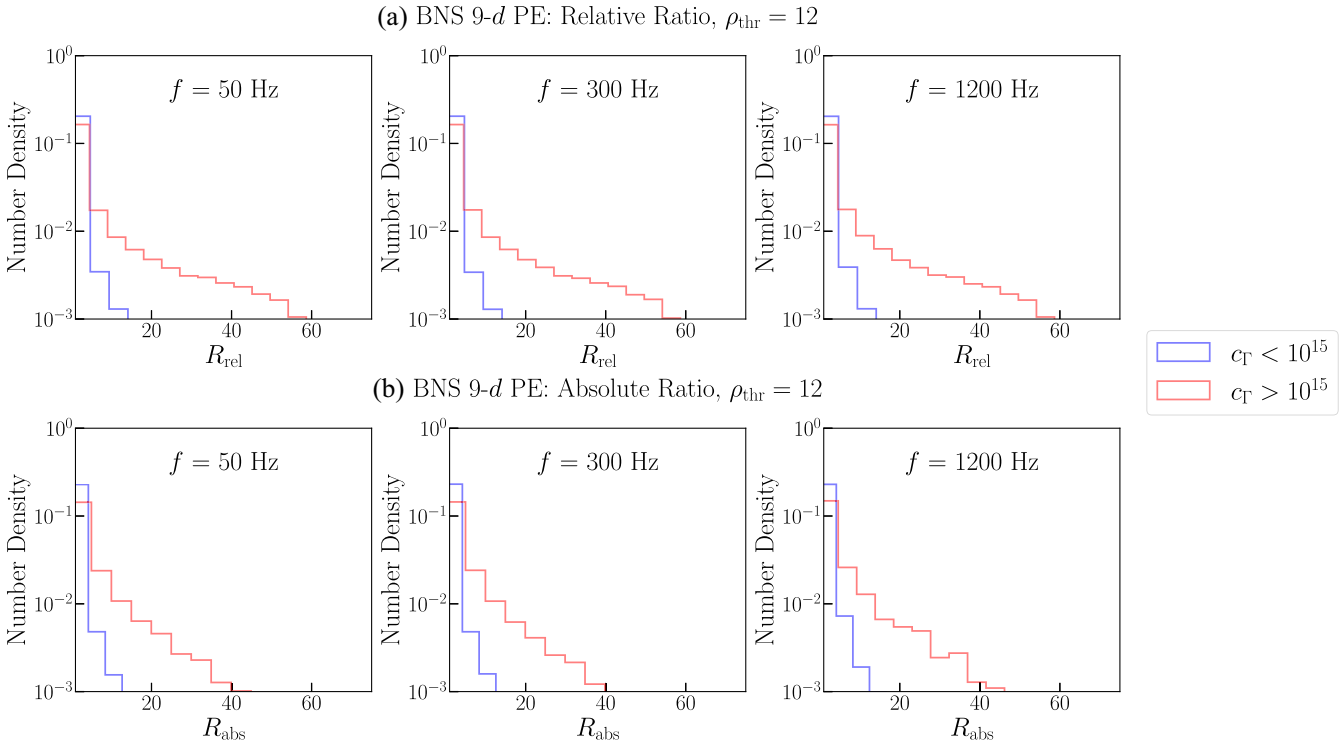

FIG. 3. Subfigure (a) shows number density distribution of the relative ratio $R_{\rm rel}$ and subfigure (b) shows absolute ratio $R_{\rm abs}$. Both subfigures show results for the BNS 9-d PE case with $\rho_{\rm thr} = 12$. Plots for events with high/low c_Γ values (denoted with red/blue color) are shown separately. Three frequency bins are chosen for illustration. The distributions at 10, 100, 200, 400, 800, and 2000 Hz have similar features, which are not shown here.

results in Zhou *et al.* [44], and we find similar features that $\Omega_{\rm err}$ increases with $\rho_{\rm thr}$ while $\Omega_{\rm ns}$ decreases with it.

However, the spectra $\Omega_{\rm err}$ in the left panels of Fig. 2 with TREATMENT (II) are greater than that in Zhou *et al.* [44], especially for the BNS 9-d PE case. This is due to the contribution from events with $c_\Gamma > 10^{15}$ in our TREATMENT (II). Those events with high c_Γ values can lead to worse subtraction results, thus contributing more to the spectrum $\Omega_{\rm err}$, compared with the events with low c_Γ values. To see it more clearly, we define two ratios for the ith event: the relative ratio $R_{\rm rel}$ and the absolute ratio $R_{\rm abs}$,

$$R_{\rm rel} = \frac{\delta h_i^2}{h_i^2}, \qquad R_{\rm abs} = \frac{\delta h_i^2}{\overline{h^2}}, \tag{21}$$

with

$$\delta h_i^2 = |\tilde{h}_+(\boldsymbol{\theta}^i_{\rm tr}; f) - \tilde{h}_+(\boldsymbol{\theta}^i_{\rm rec}; f)|^2 + |\tilde{h}_\times(\boldsymbol{\theta}^i_{\rm tr}; f) - \tilde{h}_\times(\boldsymbol{\theta}^i_{\rm rec}; f)|^2, \tag{22}$$

$$h_i^2 = |\tilde{h}_+(\boldsymbol{\theta}^i_{\rm tr}; f)|^2 + |\tilde{h}_\times(\boldsymbol{\theta}^i_{\rm tr}; f)|^2, \tag{23}$$

$$\overline{h^2} = \frac{1}{N}\sum_{i=1}^{N} h_i^2. \tag{24}$$

Notice that $\Omega_{\rm err} \propto \sum_{i=1}^{N_s} \delta h_i^2$ and $\Omega_{\rm tot} \propto \sum_{i=1}^{N} h_i^2$. The value of $R_{\rm rel}$ represents the ratio of an event's contribution to $\Omega_{\rm err}$ over its contribution to $\Omega_{\rm tot}$. Considering that the value of h_i^2 varies from event to event, we employ $R_{\rm abs}$ to estimate the ratio of an event's contribution to $\Omega_{\rm err}$ over the average contribution to $\Omega_{\rm tot}$ across all N CBC events.

We show the number density distribution of $R_{\rm rel}$ and $R_{\rm abs}$ for events with high and low c_Γ values separately in Fig. 3 for the BNS 9-d PE case with $\rho_{\rm thr} = 12$. Without loss of generality, three frequency bins are selected from low to high for illustration. We observe that events with high c_Γ values (red line) are more concentrated at higher ratio values than events with low c_Γ values (blue line) for both $R_{\rm rel}$ and $R_{\rm abs}$ at all chosen frequency bins. This indicates that events with high c_Γ values have a higher probability of resulting in a worse subtraction than events with low c_Γ values. As shown in Table I, since there are 21.98% events with high c_Γ values for BNS events with $\rho_{\rm thr} = 12$, owing to the cumulative effects of these events, we observe a larger $\Omega_{\rm err}$ in TREATMENT (II) compared to that in

TABLE I. Percentage of BBH and BNS events with $c_\Gamma > 10^{15}$ in our simulation. For BBH cases we set $\rho_{\rm thr} = 8$, while for BNS cases, we set $\rho_{\rm thr} = 12$.

	9-d PE	11-d PE
BBH	1.76%	4.32%
BNS	21.98%	58.24%

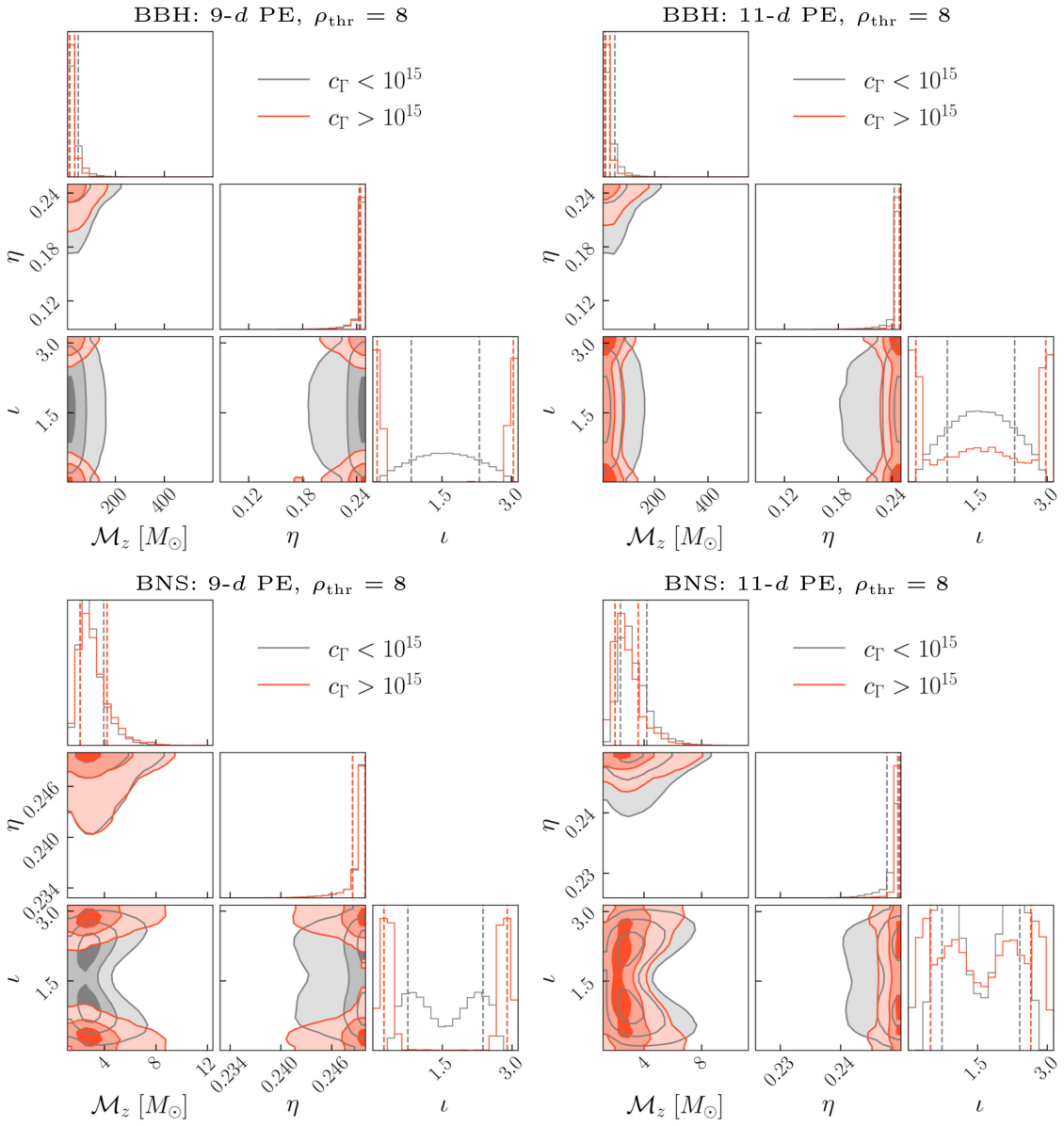

FIG. 4. Parameter distributions of events with high and low c_Γ values in four PE cases. In this figure, we set $\rho_{\rm thr} = 8$ for BBH cases and $\rho_{\rm thr} = 12$ for BNS cases. We show three parameters here: chirp mass in the observer frame $\mathcal{M}_z$, symmetric mass ratio η, and orbital inclination angle ι. Red color denotes events with $c_\Gamma > 10^{15}$, while gray color denotes events with $c_\Gamma < 10^{15}$.

TREATMENT (I). Similar results are obtained for the other three PE cases. Thus, adopting TREATMENT (I) rather than TREATMENT (II) results in an underestimation of $\Omega_{\rm err}$.

Furthermore, in Fig. 4 we observe distinctive characteristics in the parameter space for events with high c_Γ values (denoted with red color), compared with those with low c_Γ values (denoted with gray color). We set $\rho_{\rm thr} = 8$ for BBH cases and $\rho_{\rm thr} = 12$ for BNS cases. The major difference is that the orbital inclination angle of events with high c_Γ values is likely to be distributed close to 0 or π. It is not surprising, since there is strong degeneracy between the parameter pairs, $\{\iota, d_L\}$ and $\{\psi, \phi_c\}$, when ι is close to 0 or π [77–80]. Besides, for events with high c_Γ values, the symmetric mass ratio concentrates much closer to 0.25, which means that the two masses are nearly equal.

As discussed, the use of TREATMENT (I) underestimates $\Omega_{\rm err}$, so in the following we focus on the results of TREATMENT (II). As is shown in Fig. 2, when we incorporate aligned spins in PE, the spectrum $\Omega_{\rm err}$ in the right panels grows significantly, compared with those of the 9-d PE results in the left panels. When comparing our new results in the right panels in Fig. 2 with the results in Zhou *et al.* [44], we find that the $\Omega_{\rm err}$ will even surpass the total CBC foreground $\Omega_{\rm tot}$ for both BBH and BNS cases. Specifically, for the BBH case, at 10 to 1000 Hz the $\Omega_{\rm err}$ for $\rho_{\rm thr}$ chosen as 8 and 40 will surpass the $\Omega_{\rm tot}$. While

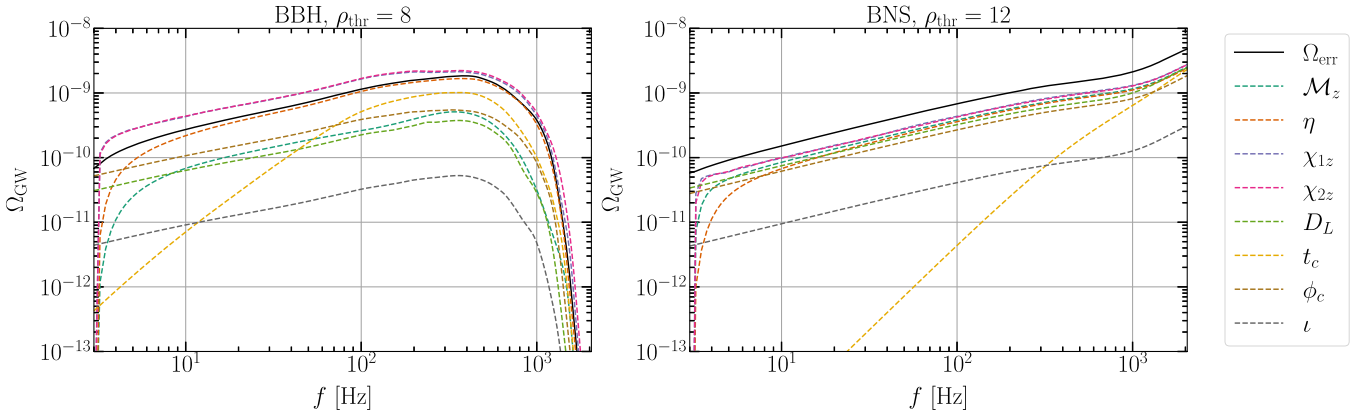

FIG. 5. Contribution from each parameter to $\Omega_{\rm err}$ for BBHs (left panel) and BNSs (right panel). Each subfigure shows $\Omega_{\rm err}$ from 11-d PE results (black solid line) and contribution from each parameter (dashed line). We choose $\rho_{\rm thr}$ equal to 8 and 12 for BBHs and BNSs respectively.

for the BNS case, the $\Omega_{\rm err}$ for $\rho_{\rm thr}$ chosen as 12 and 20 will surpass the $\Omega_{\rm tot}$ across the entire frequency band. More quantitatively, we compare the right panels of Fig. 2 with the left panels of Fig. 1, which closely follows the results from Zhou *et al.* [44]. For the BBH case, the $\Omega_{\rm err}$ for 11-d PE is approximately 3 times greater than the 9-d PE at 10 to 200 Hz, and approximately 5 to 10 times greater than the 9-d PE case at 200 to 2000 Hz, for all three chosen $\rho_{\rm thr}$. For the BNS case, we find that at 10 to 500 Hz, the $\Omega_{\rm err}$ for 11-d PE is approximately 4 times greater than the 9-d PE for $\rho_{\rm thr} = 12$, approximately 8 times greater than the 9-d PE for $\rho_{\rm thr} = 20$, and approximately 20 times greater than the 9-d PE for $\rho_{\rm thr} = 40$.

The worse subtraction results mainly come from the degeneracy between symmetric mass ratio and spins in the waveform model at the inspiral stage [81–86]. As is shown in Table II, for the BBH 11-d PE case, the absolute values of the correlation coefficients C among χ_{1z}, χ_{2z}, and η

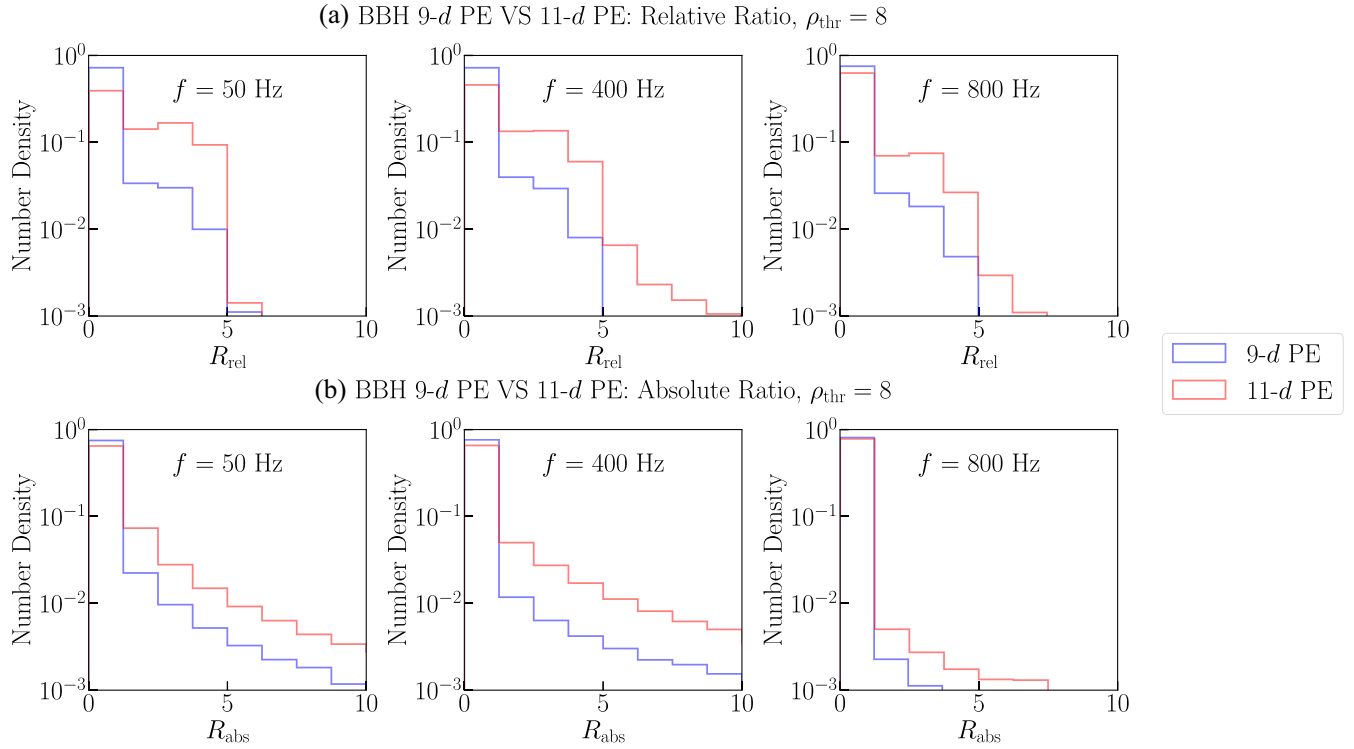

FIG. 6. Subfigure (a) shows the relative ratio $R_{\rm rel}$ and subfigure (b) shows absolute ratio $R_{\rm rel}$. Both subfigures show results for 9-d PE (blue line) and 11-d PE (red line) of BBHs. We set $\rho_{\rm thr} = 8$ and choose three frequency bins to illustrate. The BNS case has a similar feature in our simulation, which is not shown here.

TABLE II. Percentage of BBH and BNS events with the absolute values of correlation coefficients among spins and symmetric mass ratio greater than 0.99 for 11-d PE cases. For the BBH case we set $\rho_{\rm thr}=8$, and for the BNS case, $\rho_{\rm thr}=12$.

	$\lvert C_{\chi_{1z}\chi_{2z}}\rvert > 0.99$	$\lvert C_{\eta\chi_{1z}}\rvert > 0.99$	$\lvert C_{\eta\chi_{2z}}\rvert > 0.99$
BBH	98.80%	81.05%	79.98%
BNS	99.96%	84.17%	84.05%

exceed 0.99 for over 80% of all events with $\rho_{\rm thr}=8$. For the BNS 11-d PE case, over 84% of all events have correlation coefficients exceeding 0.99 with $\rho_{\rm thr}=12$. The large uncertainties due to the strong degeneracy will lead to a larger spectrum of $\Omega_{\rm err}$. To see it more clearly, we follow Zhou *et al.* [44] to estimate the contribution of each parameter to $\Omega_{\rm err}$. For each event, we reconstruct the waveform with the following choice of parameters. We first choose the kth parameter to be drawn from the 1-d Gaussian distribution with variance σ_{θ_k} (the kth diagonal component of the covariance matrix $\Sigma_{\rm net}$) when using the true value as its mean μ_{θ_k}. Then, we set all the other parameters to be their true values. Varying only one parameter and summing over all the subtracted events, we obtain $\Omega_{\rm err}$ contributed from each parameter. The results are shown in Fig. 5, where we choose $\rho_{\rm thr}$ equal to 8 and 12 for BBHs and BNSs separately. The contributions from χ_{1z}, χ_{2z}, and η dominate the spectrum $\Omega_{\rm err}$ even at such high $\rho_{\rm thr}$ values. For the BBH case, the contribution from χ_{1z} and χ_{2z} even surpasses $\Omega_{\rm err}$ from the 11-d PE results. Meanwhile, for the BNS case, there are also subdominant contributions from D_L, ϕ_c, and $\mathcal{M}_z$. Similar results were also found by Zhou *et al.* [44]. As a result, the discrepancy between parameters becomes more pronounced in the 11-d PE cases than in the 9-d PE cases. Both the relative ratio $R_{\rm rel}$ and the absolute ratio $R_{\rm abs}$ have grown significantly, compared with those in the 9-d PE cases with $\rho_{\rm thr}=8$, which is illustrated in Fig. 6 for BBHs. Hence, we observe a larger spectrum $\Omega_{\rm err}$.

As was mentioned by Zhou *et al.* [44], there exists an optimal $\rho_{\rm thr}$ to minimize the spectrum $\Omega_{\rm res}$ for the 9-d PE cases. For the 11-d PE cases, following their approach, at almost all frequency bands we find an optimal $\rho_{\rm thr}=373$ for BBHs and an optimal $\rho_{\rm thr}=200$ for BNSs to minimize the spectrum $\Omega_{\rm res}$. This implies that in our simulated populations, only 612 BBH events and seven BNS events are to be subtracted in the XG GW detector network, which is unrealistic. Therefore, a better approach is pressingly needed to deal with this issue.

IV. SUMMARY

Considering an XG detector network which includes one ET and two CEs, we estimate how well the CBC foreground can be subtracted by the FIM method, which can be used to estimate the possibility of detecting SGWB from non-CBC origins in future studies. To subtract the ith GW event whose true waveform is $\tilde{h}^i_{+/\times}(\boldsymbol{\theta}^i_{\rm tr};f)$, we first use the FIM method to approximately get the posterior distribution of the parameters. Then, we randomly draw parameters $\boldsymbol{\theta}^i_{\rm rec}$ from this distribution to reconstruct the waveform, $\tilde{h}^i_{+/\times}(\boldsymbol{\theta}^i_{\rm rec};f)$. After subtracting the reconstructed waveform, there is some residual $\delta\tilde{h}^i_{+/\times}$ in the data [see Eq. (19)]. From the summation over all the subtracted events we obtain the spectrum $\Omega_{\rm err}$, which corresponds to the energy density brought by the imperfect foreground subtraction. Then, $\Omega_{\rm err}$, combined with $\Omega_{\rm ns}$, which is the spectrum of the GW events that are not subtracted because of low SNRs, forms $\Omega_{\rm res}$. In reality, we want to minimize $\Omega_{\rm res}$ so as to detect SGWB from non-CBC origins.

As an extension of the previous studies by Sachdev *et al.* [43] and Zhou *et al.* [44], two more new features are considered during the subtraction. Firstly, we include spin parameters in PE, in other words, we adopt an 11-d PE using the FIM for the CBC events to be subtracted. For a realistic consideration, we generate 10^5 BBH and BNS events based on the latest population models provided by the LVK Collaboration [56] and consider different treatments for subtraction of events that have large condition numbers when inverting the FIM. Secondly, we discuss the effects of the extreme events with a high value of c_Γ.

When we do the subtraction, we first set a threshold SNR $\rho_{\rm thr}$. For those low SNR events with $\rho_{\rm net}<\rho_{\rm thr}$, we do not subtract them since the PE uncertainties of these events are too large, and some events are even unsolvable if $\rho_{\rm net}\lesssim 8$. However, there is still no guarantee that one can reconstruct the true waveform for an event with a large SNR well. Sometimes, there can be strong degeneracy between some parameters in the waveform model, which leads to a large deviation between the reconstructed waveform and the true waveform. When the degeneracy between the parameters is strong, the condition number c_Γ of FIM can be very large. We propose two treatments. For TREATMENT (I), we subtract the events whose $\rho_{\rm net}>\rho_{\rm thr}$ and $c_\Gamma<10^{15}$, and for TREATMENT (II), we subtract all the events as long as $\rho_{\rm net}>\rho_{\rm thr}$. Comparing the results of TREATMENT (I) in Fig. 1 and TREATMENT (II) in Fig. 2, we find significant contribution to $\Omega_{\rm err}$ from events with large c_Γ. We verify it by calculating the distribution of $R_{\rm rel}$ and $R_{\rm abs}$ [see Eq. (21)], as shown in Fig. 3. To conclude, the early study underestimated $\Omega_{\rm err}$ when discarding events with large c_Γ. To be more realistic, we include these events in our calculation. We also study the characteristics of the distribution of parameters when $\rho_{\rm net}>\rho_{\rm thr}$ and $c_\Gamma>10^{15}$. The orbital inclination angle ι is much more likely to distribute around 0 or π for these events (see Fig. 4), which leads to degeneracy between ι and D_L, and ψ and ϕ_c. Besides, the symmetric mass ratio is more likely to be closer to 0.25 for events with high c_Γ values. By introducing higher order modes in the waveform model, we may break the degeneracy between ι and D_L, and ψ and ϕ_c to some

extent [87–90], especially for the events with asymmetric masses [91,92] or high masses [93,94]. The uncertainty in PE for events with spins can also be reduced by including nonquadrupole modes [95–97]. From this perspective, we expect to get a more optimistic result of the foreground subtraction by using a waveform model including higher order modes in future studies.

We compare our results with those obtained by Zhou *et al.* [44], where a 9-d PE was adopted. After including the aligned spins, the degeneracy between parameters becomes worse, especially between the spin parameters and the symmetric mass ratio. As is shown in Fig. 5, the effects from χ_{1z}, χ_{2z} and η surpass that from ϕ_c which dominates in the 9-d PE [44]. The degeneracy increases the uncertainty when performing PE and results in unexpectedly large $\Omega_{\rm res}$, which is even larger than $\Omega_{\rm tot}$.

In this work, we only consider the uncertainty of PE brought by the noise. When the error from inaccurate waveform modeling cannot be neglected [98–101], it also needs to be discussed quantitatively in future studies. Lastly, we have assumed that GW signals can be identified and then subtracted one by one in the literature. However, it seems very optimistic for XG detectors since there can be plenty of GW signals overlapping with each other, making PE more difficult [102–108]. We have to take into account the effects of overlapping between signals in future studies.

ACKNOWLEDGMENTS

We thank Zhenwei Lyu, Xing-Jiang Zhu, Zhen Pan, Huan Yang, and the anonymous referee for helpful comments. This work was supported by the Beijing Natural Science Foundation (1242018), the National Natural Science Foundation of China (11975027, 11991053, 11721303), the China Postdoctoral Science Foundation (2021TQ0018), the National SKA Program of China (2020SKA0120300), the Max Planck Partner Group Program funded by the Max Planck Society, and the High-Performance Computing Platform of Peking University.

APPENDIX: SUPPLEMENTARY WAVEFORM SUBTRACTION METHOD AND RESULTS

In the main context, following the methods from Sachdev *et al.* [43] and Zhou *et al.* [44], we obtain the residual for each event by subtracting the reconstructed plus and cross GW polarization waveforms from the true waveforms. Additionally, we introduce a supplementary subtraction method from Cutler and Harms [21] and Pan and Yang [46]. In this method, the primary residual is obtained by subtracting the reconstructed strain from the true strain recorded in the detector. We still use the same parameter basis as the main context rather than the reparametrization basis in Pan and Yang [46]. The strain signal for a specific event is

$$H(\boldsymbol{\theta}; f) = F_+(\alpha, \delta, \psi)\tilde{h}_+(f) + F_\times(\alpha, \delta, \psi)\tilde{h}_\times(f), \tag{A1}$$

where F_+ and $F_\times$ are the antenna pattern functions of the detector. Then, the energy flux can be expressed in terms of GW strain signal as [46]

$$F_{\rm tot}(f) = \frac{2}{\langle F_+^2\rangle + \langle F_\times^2\rangle}\frac{\pi c^3}{2G}\frac{f^2}{T}\sum_{i=1}^{N}|H^i(f)|^2, \tag{A2}$$

where $\langle F_+^2\rangle$ and $\langle F_\times^2\rangle$ are the angle-averaged antenna pattern functions. Following the discussion in Pan and Yang [46], a CE with a 40-km arm located in Idaho, U.S., was considered as the reference detector. For such an L-shaped interferometer, $\langle F_+^2\rangle = \langle F_\times^2\rangle = \frac{1}{5}$. When it comes to the foreground subtraction, the residual for each event is

$$\delta H^i(f) = H^i(\boldsymbol{\theta}^i_{\rm tr}, f) - H^i(\boldsymbol{\theta}^i_{\rm rec}, f), \tag{A3}$$

where the recovered parameters $\boldsymbol{\theta}^i_{\rm rec}$ are obtained by the FIM methods using TREATMENT (II). Then, the energy flux due to imperfect subtraction is

$$F_{\rm err}(f) = \frac{2}{\langle F_+^2\rangle + \langle F_\times^2\rangle}\frac{\pi c^3}{2G}\frac{f^2}{T}\sum_{i=1}^{N_s}|\delta H^i(f)|^2 \tag{A4}$$

and the flux for $N_{\rm ns}$ unsubtracted events is

$$F_{\rm ns} = \frac{\pi c^3}{2G}\frac{f^2}{T}\sum_{i=1}^{N_{\rm ns}}|H^i(f)|^2. \tag{A5}$$

To illustrate, we consider the same BBH population as in the main text for calculating the $\Omega_{\rm ns}$ and $\Omega_{\rm err}$. The results are shown in Fig. 7, in which we plot the $\Omega_{\rm ns}$ and $\Omega_{\rm err}$ for the main method as red color and for the supplementary method as blue color. Both the 9-d PE case and the 11-d case are considered. We also show the comparison of these two methods in the bottom panels for $\Omega_{\rm err}$ against $\Omega_{\rm tot}$. Since we want a better foreground subtraction, a smaller value is preferred. There are slight differences for the $\Omega_{\rm tot}$ in two methods because of the different treatments of α, δ, ψ in Eq. (A4) and Eq. (16). We find that for the 9-d PE case, the supplementary subtraction method gives more positive results than the main method for approximately 3 times at 10 to 1000 Hz. For the 11-d case, the main method gives more positive results than the supplementary subtraction method for approximately 2 times around 10 to 1000 Hz. Meanwhile, the supplementary subtraction method for 11-d PE case also shows that the $\Omega_{\rm err}$ surpasses the $\Omega_{\rm tot}$ at 10 to 1000 Hz, which is consistent with our results in the main text. Moreover, since in the results of the 11-d PE case, the main method shows a slightly better subtraction effect, we consider the results in the main text quite complementary to the methods in other works.

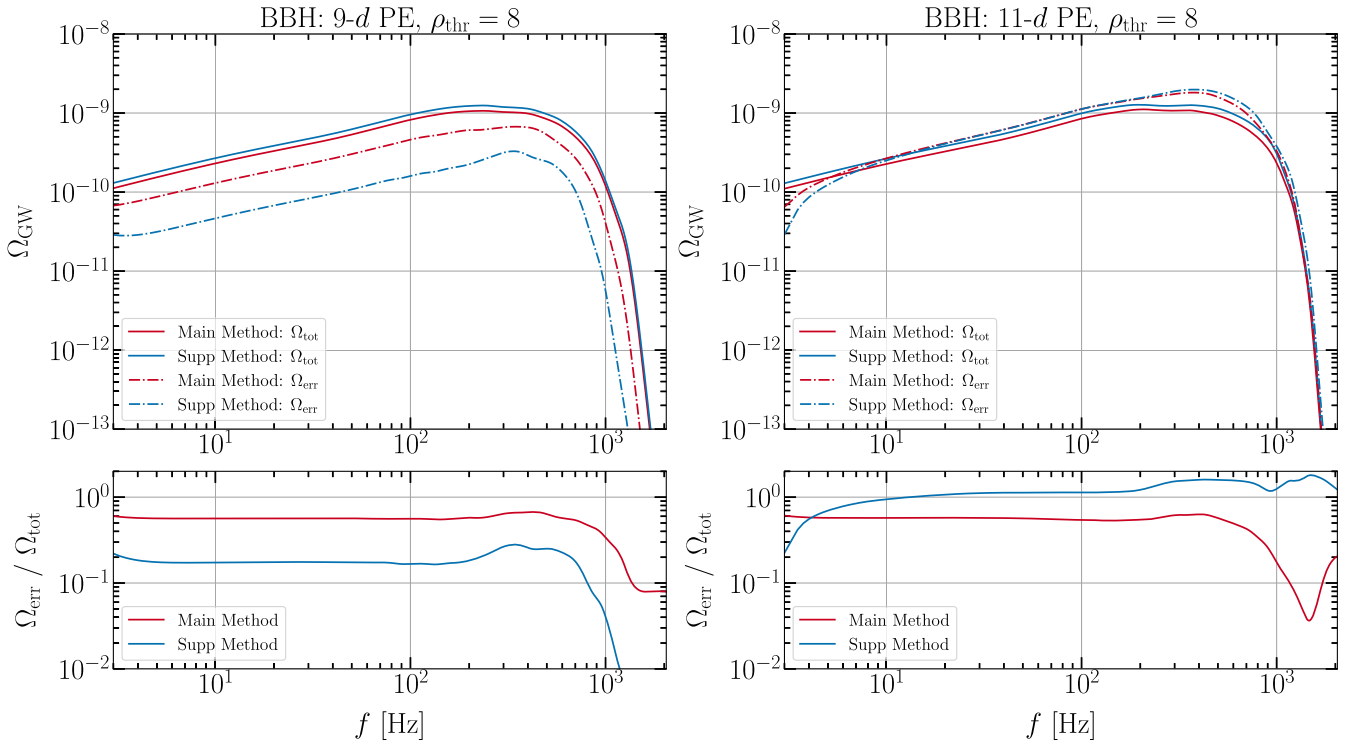

FIG. 7. The foreground subtraction results are presented for the main method (from main text) with red color and the supplementary method (from this Appendix) with blue color. The left panels show the results for 9-d PE, while the right panels show the results for 11-d PE. In the top panels, each subfigure shows the $\Omega_{\rm tot}$ with solid line and $\Omega_{\rm err}$ with $\rho_{\rm thr} = 8$ with a dash-dotted line. In the bottom panels, each subfigure shows the results of $\Omega_{\rm err}$ against $\Omega_{\rm tot}$.

[1] R. W. Hellings and G. S. Downs, Astrophys. J. Lett. **265**, L39 (1983).
[2] G. Agazie *et al.* (NANOGrav Collaboration), Astrophys. J. Lett. **951**, L9 (2023).
[3] G. Agazie *et al.* (NANOGrav Collaboration), Astrophys. J. Lett. **951**, L8 (2023).
[4] J. Antoniadis *et al.* (EPTA Collaboration), Astron. Astrophys. **678**, A48 (2023).
[5] J. Antoniadis *et al.* (EPTA Collaboration), Astron. Astrophys. **678**, A49 (2023).
[6] J. Antoniadis *et al.* (EPTA Collaboration), Astron. Astrophys. **678**, A50 (2023).
[7] A. Zic *et al.*, Pub. Astron. Soc. Aust. **40**, e049 (2023).
[8] D. J. Reardon *et al.*, Astrophys. J. Lett. **951**, L6 (2023).
[9] H. Xu *et al.*, Res. Astron. Astrophys. **23**, 075024 (2023).
[10] N. Christensen, Rep. Prog. Phys. **82**, 016903 (2019).
[11] M. S. Turner, Phys. Rev. D **55**, R435 (1997).
[12] X. Siemens, V. Mandic, and J. Creighton, Phys. Rev. Lett. **98**, 111101 (2007).
[13] T. Damour and A. Vilenkin, Phys. Rev. D **71**, 063510 (2005).
[14] C. Caprini, R. Durrer, and G. Servant, Phys. Rev. D **77**, 124015 (2008).
[15] A. Kosowsky, M. S. Turner, and R. Watkins, Phys. Rev. D **45**, 4514 (1992).
[16] S. J. Huber and T. Konstandin, J. Cosmol. Astropart. Phys. 09 (2008) 022.
[17] S.-L. Li, L. Shao, P. Wu, and H. Yu, Phys. Rev. D **104**, 043510 (2021).
[18] Z.-C. Chen, S.-L. Li, P. Wu, and H. Yu, Phys. Rev. D **109**, 043022 (2024).
[19] C. L. Fryer and K. C. B. New, Living Rev. Relativity **14**, 1 (2011).
[20] K. Crocker, T. Prestegard, V. Mandic, T. Regimbau, K. Olive, and E. Vangioni, Phys. Rev. D **95**, 063015 (2017).
[21] C. Cutler and J. Harms, Phys. Rev. D **73**, 042001 (2006).
[22] X.-J. Zhu, E. J. Howell, D. G. Blair, and Z.-H. Zhu, Mon. Not. R. Astron. Soc. **431**, 882 (2013).
[23] X.-J. Zhu, E. Howell, T. Regimbau, D. Blair, and Z.-H. Zhu, Astrophys. J. **739**, 86 (2011).
[24] E. S. Phinney, arXiv:astro-ph/0108028.
[25] P. A. Rosado, Phys. Rev. D **84**, 084004 (2011).

[26] B. P. Abbott *et al.* (LIGO Scientific and VIRGO Collaborations), Nature (London) **460**, 990 (2009).
[27] B. P. Abbott *et al.* (LIGO Scientific and VIRGO Collaborations), Phys. Rev. Lett. **118**, 121101 (2017); **119**, 029901(E) (2017).
[28] R. Abbott *et al.* (KAGRA, Virgo, and LIGO Scientific Collaborations), Phys. Rev. D **104**, 022004 (2021).
[29] R. Abbott *et al.* (KAGRA, Virgo, and LIGO Scientific Collaborations), Phys. Rev. X **13**, 041039 (2023).
[30] B. P. Abbott *et al.* (LIGO Scientific and VIRGO Collaborations), Phys. Rev. X **9**, 031040 (2019).
[31] R. Abbott *et al.* (LIGO Scientific and VIRGO Collaborations), Phys. Rev. X **11**, 021053 (2021).
[32] R. Abbott *et al.* (LIGO Scientific and VIRGO Collaborations), Phys. Rev. D **109**, 022001 (2024).
[33] A. H. Nitz, S. Kumar, Y.-F. Wang, S. Kastha, S. Wu, M. Schäfer, R. Dhurkunde, and C. D. Capano, Astrophys. J. **946**, 59 (2023).
[34] S. Olsen, T. Venumadhav, J. Mushkin, J. Roulet, B. Zackay, and M. Zaldarriaga, Phys. Rev. D **106**, 043009 (2022).
[35] M. Punturo *et al.*, Classical Quantum Gravity **27**, 194002 (2010).
[36] B. S. Sathyaprakash *et al.*, Bull. Am. Astron. Soc. **51**, 251 (2019).
[37] D. Reitze *et al.*, Bull. Am. Astron. Soc. **51**, 035 (2019), https://ui.adsabs.harvard.edu/abs/2019BAAS...51g..35R/abstract.
[38] V. Kalogera *et al.*, arXiv:2111.06990.
[39] S. Borhanian and B. S. Sathyaprakash, arXiv:2202.11048.
[40] S. Ronchini, M. Branchesi, G. Oganesyan, B. Banerjee, U. Dupletsa, G. Ghirlanda, J. Harms, M. Mapelli, and F. Santoliquido, Astron. Astrophys. **665**, A97 (2022).
[41] F. Iacovelli, M. Mancarella, S. Foffa, and M. Maggiore, Astrophys. J. **941**, 208 (2022).
[42] T. Regimbau, M. Evans, N. Christensen, E. Katsavounidis, B. Sathyaprakash, and S. Vitale, Phys. Rev. Lett. **118**, 151105 (2017).
[43] S. Sachdev, T. Regimbau, and B. S. Sathyaprakash, Phys. Rev. D **102**, 024051 (2020).
[44] B. Zhou, L. Reali, E. Berti, M. Çalışkan, C. Creque-Sarbinowski, M. Kamionkowski, and B. S. Sathyaprakash, Phys. Rev. D **108**, 064040 (2023).
[45] H. Zhong, R. Ormiston, and V. Mandic, Phys. Rev. D **107**, 064048 (2023).
[46] Z. Pan and H. Yang, Phys. Rev. D **107**, 123036 (2023).
[47] D. S. Bellie, S. Banagiri, Z. Doctor, and V. Kalogera, arXiv:2310.02517.
[48] S. Biscoveanu, C. Talbot, E. Thrane, and R. Smith, Phys. Rev. Lett. **125**, 241101 (2020).
[49] V. Kalogera, Astrophys. J. **541**, 319 (2000).
[50] I. Mandel and R. O'Shaughnessy, Classical Quantum Gravity **27**, 114007 (2010).
[51] M. Dominik, K. Belczynski, C. Fryer, D. E. Holz, E. Berti, T. Bulik, I. Mandel, and R. O'Shaughnessy, Astrophys. J. **779**, 72 (2013).
[52] J. J. Eldridge, E. R. Stanway, L. Xiao, L. A. S. McClelland, G. Taylor, M. Ng, S. M. L. Greis, and J. C. Bray, Pub. Astron. Soc. Aust. **34**, e058 (2017).
[53] N. Giacobbo, M. Mapelli, and M. Spera, Mon. Not. R. Astron. Soc. **474**, 2959 (2018).
[54] A. Olejak, M. Fishbach, K. Belczynski, D. E. Holz, J. P. Lasota, M. C. Miller, and T. Bulik, Astrophys. J. Lett. **901**, L39 (2020).
[55] R. Abbott *et al.* (LIGO Scientific and VIRGO Collaborations), Astrophys. J. Lett. **913**, L7 (2021).
[56] R. Abbott *et al.* (KAGRA, Virgo, and LIGO Scientific Collaborations), Phys. Rev. X **13**, 011048 (2023).
[57] D. Bhattacharya and E. P. J. van den Heuvel, Phys. Rep. **203**, 1 (1991).
[58] X.-J. Zhu and G. Ashton, Astrophys. J. Lett. **902**, L12 (2020).
[59] C. L. Rodriguez, I. Mandel, and J. R. Gair, Phys. Rev. D **85**, 062002 (2012).
[60] M. Vallisneri, Phys. Rev. D **77**, 042001 (2008).
[61] S. Borhanian, Classical Quantum Gravity **38**, 175014 (2021).
[62] T. mpmath development team, mpmath: a Python library for arbitrary-precision floating-point arithmetic (version 1.3.0) (2023), http://mpmath.org/.
[63] S. Husa, S. Khan, M. Hannam, M. Pürrer, F. Ohme, X. Jiménez Forteza, and A. Bohé, Phys. Rev. D **93**, 044006 (2016).
[64] S. Khan, S. Husa, M. Hannam, F. Ohme, M. Pürrer, X. Jiménez Forteza, and A. Bohé, Phys. Rev. D **93**, 044007 (2016).
[65] E. Vangioni, K. A. Olive, T. Prestegard, J. Silk, P. Petitjean, and V. Mandic, Mon. Not. R. Astron. Soc. **447**, 2575 (2015).
[66] E. Nakar, Phys. Rep. **442**, 166 (2007).
[67] M. Dominik, K. Belczynski, C. Fryer, D. Holz, E. Berti, T. Bulik, I. Mandel, and R. O'Shaughnessy, Astrophys. J. **759**, 52 (2012).
[68] B. P. Abbott *et al.* (LIGO Scientific and VIRGO Collaborations), Phys. Rev. Lett. **116**, 131102 (2016).
[69] B. P. Abbott *et al.* (LIGO Scientific and VIRGO Collaborations), Phys. Rev. Lett. **120**, 091101 (2018).
[70] D. Meacher, M. Coughlin, S. Morris, T. Regimbau, N. Christensen, S. Kandhasamy, V. Mandic, J. D. Romano, and E. Thrane, Phys. Rev. D **92**, 063002 (2015).
[71] T. Callister, L. Sammut, S. Qiu, I. Mandel, and E. Thrane, Phys. Rev. X **6**, 031018 (2016).
[72] B. P. Abbott *et al.* (LIGO Scientific and VIRGO Collaborations), Astrophys. J. Lett. **882**, L24 (2019).
[73] N. Farrow, X.-J. Zhu, and E. Thrane, Astrophys. J. **876**, 18 (2019).
[74] E. Berti, A. Buonanno, and C. M. Will, Phys. Rev. D **71**, 084025 (2005).
[75] Z. Lyu, N. Jiang, and K. Yagi, Phys. Rev. D **105**, 064001 (2022).
[76] L. S. Finn, Phys. Rev. D **46**, 5236 (1992).
[77] C. Cutler and E. E. Flanagan, Phys. Rev. D **49**, 2658 (1994).
[78] J. Aasi *et al.* (LIGO Scientific and VIRGO Collaborations), Phys. Rev. D **88**, 062001 (2013).
[79] J. Veitch *et al.*, Phys. Rev. D **91**, 042003 (2015).
[80] S. A. Usman, J. C. Mills, and S. Fairhurst, Astrophys. J. **877**, 82 (2019).
[81] E. Baird, S. Fairhurst, M. Hannam, and P. Murphy, Phys. Rev. D **87**, 024035 (2013).

[82] M. Hannam, D. A. Brown, S. Fairhurst, C. L. Fryer, and I. W. Harry, Astrophys. J. Lett. **766**, L14 (2013).
[83] F. Ohme, A. B. Nielsen, D. Keppel, and A. Lundgren, Phys. Rev. D **88**, 042002 (2013).
[84] C. P. L. Berry *et al.*, Astrophys. J. **804**, 114 (2015).
[85] M. Pürrer, M. Hannam, and F. Ohme, Phys. Rev. D **93**, 084042 (2016).
[86] B. Farr *et al.*, Astrophys. J. **825**, 116 (2016).
[87] P. D. Lasky, E. Thrane, Y. Levin, J. Blackman, and Y. Chen, Phys. Rev. Lett. **117**, 061102 (2016).
[88] E. Payne, C. Talbot, and E. Thrane, Phys. Rev. D **100**, 123017 (2019).
[89] C. Zhang, N. Dai, and D. Liang, Phys. Rev. D **108**, 044076 (2023).
[90] Y. Gong, Z. Cao, J. Zhao, and L. Shao, Phys. Rev. D **108**, 064046 (2023).
[91] R. Abbott *et al.* (LIGO Scientific and VIRGO Collaborations), Phys. Rev. D **102**, 043015 (2020).
[92] R. Abbott *et al.* (LIGO Scientific and VIRGO Collaborations), Astrophys. J. Lett. **896**, L44 (2020).
[93] K. Chatziioannou *et al.*, Phys. Rev. D **100**, 104015 (2019).
[94] R. Abbott *et al.* (LIGO Scientific and VIRGO Collaborations), Astrophys. J. Lett. **900**, L13 (2020).
[95] V. Varma, P. Ajith, S. Husa, J. C. Bustillo, M. Hannam, and M. Pürrer, Phys. Rev. D **90**, 124004 (2014).
[96] J. Calderón Bustillo, S. Husa, A. M. Sintes, and M. Pürrer, Phys. Rev. D **93**, 084019 (2016).
[97] V. Varma and P. Ajith, Phys. Rev. D **96**, 124024 (2017).
[98] C. Cutler and M. Vallisneri, Phys. Rev. D **76**, 104018 (2007).
[99] R. Gamba, M. Breschi, S. Bernuzzi, M. Agathos, and A. Nagar, Phys. Rev. D **103**, 124015 (2021).
[100] M. Pürrer and C.-J. Haster, Phys. Rev. Res. **2**, 023151 (2020).
[101] Q. Hu and J. Veitch, Astrophys. J. **945**, 103 (2023).
[102] T. Regimbau *et al.*, Phys. Rev. D **86**, 122001 (2012).
[103] D. Meacher, K. Cannon, C. Hanna, T. Regimbau, and B. S. Sathyaprakash, Phys. Rev. D **93**, 024018 (2016).
[104] A. Samajdar, J. Janquart, C. Van Den Broeck, and T. Dietrich, Phys. Rev. D **104**, 044003 (2021).
[105] E. Pizzati, S. Sachdev, A. Gupta, and B. Sathyaprakash, Phys. Rev. D **105**, 104016 (2022).
[106] P. Relton and V. Raymond, Phys. Rev. D **104**, 084039 (2021).
[107] Z. Wang, D. Liang, J. Zhao, C. Liu, and L. Shao, Classical Quantum Gravity **41**, 055011 (2024).
[108] Y. Dang, Z. Wang, D. Liang, and L. Shao, Astrophys. J. **964**, 194 (2024).